Separation and Purification Technology 320 (2023) 124109

Contents lists available at ScienceDirect

Separation and Purification Technology

journal homepage: www.elsevier.com/locate/seppur

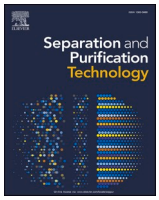

A robust perylene diimide-based zirconium metal–organic framework for preferential adsorption of ethane over ethylene

Jing-Jing Li [a], Si-Yi Liu [a], Guoliang Liu [a,*], Yu-Guo Liu [a], Guan-Zhou Wu [a], Hua-Dong Li [a], Rajamani Krishna [b], Xiao-Qin Liu [a], Lin-Bing Sun [a,*]

[a] State Key Laboratory of Materials-Oriented Chemical Engineering, Jiangsu National Synergetic Innovation Center for Advanced Material (SICAM), College of Chemical Engineering, Nanjing Tech University, Nanjing 211816, China
[b] Van't Hoff Institute for Molecular Sciences, University of Amsterdam, Science Park 904, 1098 XH Amsterdam, Netherlands

ARTICLE INFO

Keywords:
Gas separation
Metal–organic frameworks
C_2H_6-selective adsorbent
C_2H_4 purification
Stability

ABSTRACT

Adsorptive separation of ethane (C_2H_6)/ ethylene (C_2H_4) mixtures based on C_2H_6-selective adsorbents through one-step separation unit has attracted great attention in view of its enormous potential to reduce energy consumption in the petrochemical industry. To achieve this, it is highly demanded to develop C_2H_6-selective adsorbents. However, it is challenging to construct C_2H_6-selective adsorbents due to the difficulty in building suitable interaction between C_2H_6 molecules and adsorption active sites. Here, we constructed a robust perylene diimide-based zirconium metal–organic framework (MOF, denoted as Zr-Me-PDI) of superior stability under aqueous solution of different pH values (1.0 ~ 10.0), for effectively separation of C_2H_6 from C_2H_4. Zr-Me-PDI displayed C_2H_6-selective adsorption behavior at both 298 and 273 K. High C_2H_6 adsorption capacity 3.9 mmol·g^{-1} and C_2H_6/C_2H_4 selectivity (1.5) was achieved for Zr-Me-PDI at 1 bar and 298 K, comparable to most of the high-performance C_2H_6-selective MOFs. Calculation results of Grand Canonical Monte Carlo (GCMC) simulation show that the interpenetrated structure of Zr-Me-PDI exhibit multiple C-H···Cl and C-H···O interactions with C_2H_6 and preferentially binds to C_2H_6 over C_2H_4. Therefore, the results demonstrated in this project may provide valuable guidance for the design and synthesis of C_2H_6-selective adsorbents.

1. Introduction

Ethylene (C_2H_4) is a significant chemical raw material commonly used in industry, which can be further transformed into more useful consumer goods and industrial products. At present, the main production processes of C_2H_4 include steam cracking, methanol to olefin, and ethane (C_2H_6) dehydrogenation [1,2]. In these processes, the products will simultaneously contain C_2H_6 and C_2H_4. However, it is difficult to obtain C_2H_4 with desired purity because the properties of C_2H_6 and C_2H_4 has a close resemblance (such as boiling point and kinetic diameter) [3-6]. To date, heat-driven procedures, such as low-temperature distillation is still the traditional method for industrial separation of C_2H_6/C_2H_4 mixtures, typically utilizing distillation column composed of over 150 trays at relative hostile temperature and pressure conditions (-25 ℃ and 23 bar) [7,8]. However, this essential procedure is a high cost and very energy-intensive process. In this case, in order to meet the industrial demand for C_2H_6/C_2H_4 mixture separation, it is urgent to develop an efficient separation technology with low energy consumption.

Due to the merits of easy operation, energy saving and environmentally sound, the adsorptive separation technology has a good application prospect for gas separation [9-13]. Adsorbents including zeolites, clay-based materials, silica, carbon-based materials, hydrogen-bonded organic framework, and metal–organic frameworks (MOFs) are generally used for C_2H_6 and C_2H_4 separation [14-22]. In general, there are two sorts of adsorbents for C_2H_6/C_2H_4 selective separation, namely C_2H_4-selective adsorbents and C_2H_6-selective ones [23]. Most of the adsorbents preferentially adsorb C_2H_4 for the larger quadrupole moment and π electron presence of C_2H_4 molecule, making its interaction with metal sites/clusters stronger [24-26]. However, for C_2H_4-selective adsorbents, desorption of C_2H_4 gas is required after the priority of C_2H_4 adsorption. This process needs at least 4 adsorption–desorption cycles to obtain polymer-grade C_2H_4 of 99.95% purity, giving rise to vast energy consumption [27]. For C_2H_6-selective adsorbents, the adsorbents can preferentially adsorb C_2H_6, and the required high-purity C_2H_4 products

* Corresponding authors at: State Key Laboratory of Materials-Oriented Chemical Engineering, Jiangsu National Synergetic Innovation Center for Advanced Material (SICAM), College of Chemical Engineering, Nanjing Tech University, Nanjing 211816, China.
E-mail addresses: glliu@njtech.edu.cn (G. Liu), lbsun@njtech.edu.cn (L.-B. Sun).

https://doi.org/10.1016/j.seppur.2023.124109
Received 8 February 2023; Received in revised form 13 May 2023; Accepted 13 May 2023
Available online 18 May 2023

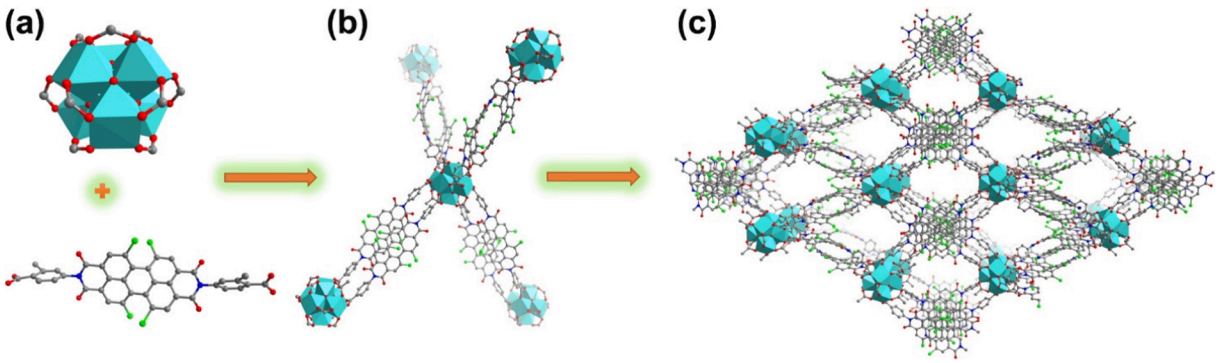

Fig. 1. (a) Structures of Zr-cluster and PDI-Me-COOH. (b) Coordination environment of Zr-clusters. (c) Crystal structure of Zr-Me-PDI. Color code: Zr, blue; C, grey; Cl, green; O, red; and N, blue.

will be directly recovered during 1 adsorption–desorption cycle (Figure S1). Compared to C_2H_4-selective adsorbent, the usage of C_2H_6-selective adsorbents is capable of saving about 40 % of energy (0.4 to 0.6 GJ/ton of C_2H_4) [28]. Albeit highly expected, it is challenge to construct C_2H_6-selective adsorbents due to the difficulty in building suitable interaction between C_2H_6 molecules and adsorption active sites.

Derivatives of perylene 3, 4, 9, 10-tetracarboxylic acid diamine (PDI) have received extensive attention from academia and industry. PDI derivatives are a class of compounds with special thick ring structures. Besides, PDI also feature multiple carboxyl and chloride functional groups. Construction of MOFs with PDI motifs show potentials as C_2H_6-selective adsorbents due to the potentially abundant C-H···O, C-H···π, and C-H···Cl interplays between PDI motifs and C_2H_6 molecules. In this paper, we reported a robust PDI-based Zr MOF (denoted as Zr-Me-PDI) for C_2H_6/C_2H_4 mixture separation. Zr-Me-PDI displayed remarkable C_2H_6-selective adsorption behavior with C_2H_6/C_2H_4 selectivity is 1.5 and the C_2H_6 adsorption capacity can be as high as 3.9 mmol·g^{-1} at 1 bar and 298 K. Grand Canonical Monte Carlo (GCMC) simulations have cooperatively verified its reversed adsorption behavior for preferentially trapping C_2H_6 molecule. Besides, Zr-Me-PDI showed excellent water stability under aqueous solutions of different pH values. The detailed analysis may provide valuable guidance for the design and synthesis of PDI-based adsorbents for selective C_2H_6/C_2H_4 separation.

2. Experimental section

2.1. Preparation of Zr-Me-PDI

Zr-Me-PDI was first synthesized via solvothermal reaction of $ZrCl_4$ (51.6 mg, 0.216 mmol) and N, N'-bis-(2-methyl-4-benzoic acid)-1, 2, 6,

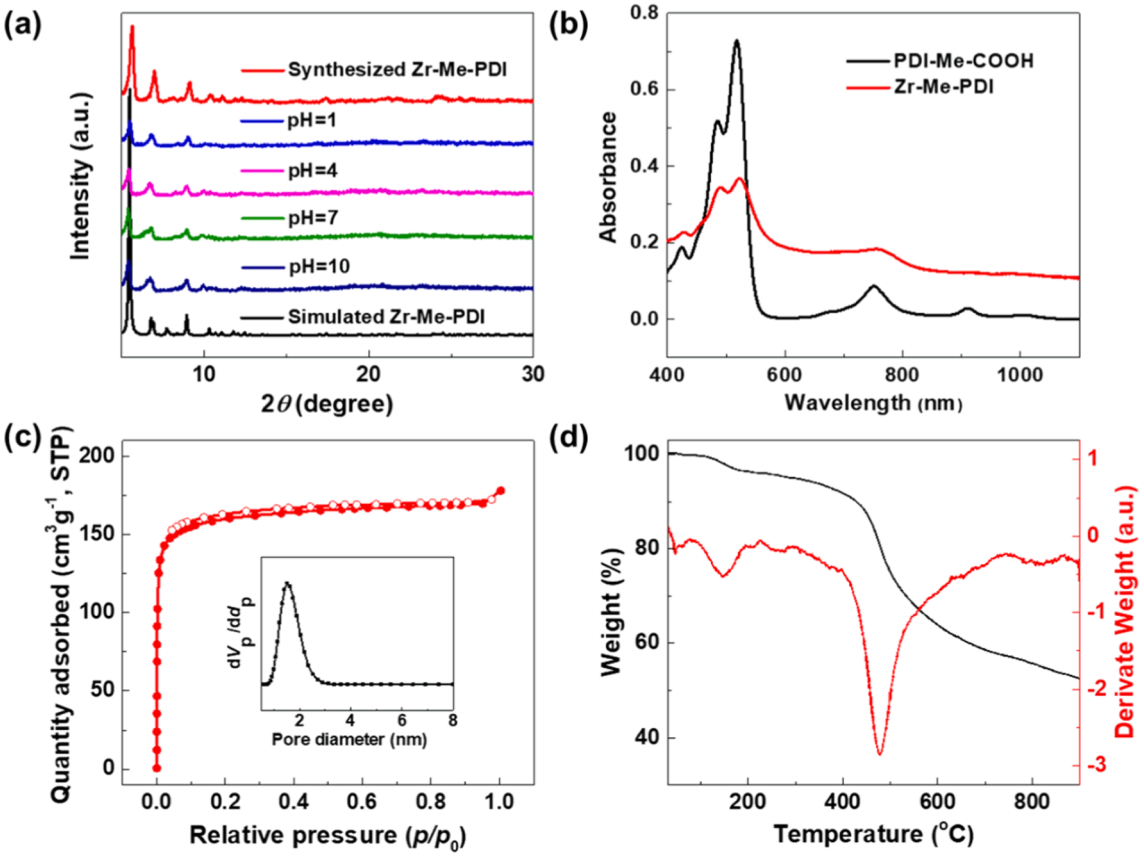

Fig. 2. (a) PXRD patterns of Zr-Me-PDI and the samples treated under aqueous solutions of varied pH values. (b) UV–Vis-NIR analysis of PDI-Me-COOH ligand and Zr-Me-PDI. (c) Standard N_2 analysis for Zr-Me-PDI at 77 K (Insert: pore size distributions based on NLDFT model). (d) TGA and DTG curves of Zr-Me-PDI.

7-tetrachloropylene-3, 4, 9, 10-tetracarboxylic acid diimide (PDI-Me-COOH, Scheme S1 and Figure S2) ligand (168.6 mg, 0.216 mmol) in N, N-dimethylformamide (DMF, 20.0 mL) and acetic acid (5.4 mL). The reaction reagents were added into a 50.0 mL covered vial after sonication, and then heated at 363 K. The mixture was slowly cooled to room temperature after 3 days. Red crystals were collected through filtration. The obtained crystals were washed thrice utilizing fresh DMF and acetone, and then dried it under vacuum at 373 K for 24 h to obtain Zr-Me-PDI.

2.2. Gas adsorption measurement

Standard N_2 sorption isotherm was measured with liquid nitrogen at 77 K using a Micromeritics ASAP 2020 analyzer. Adsorption isotherms for C_2H_6 and C_2H_4 were also collected at 273 and 298 K on an ASAP 2020 analyzer. The sample tube was immersed in ice bath and water bath for well control of adsorption temperature. Before the measurement, about 70 mg of activated Zr-Me-PDI was further degassed on the ASAP 2020 analyzer at 423 K for 6 h. For cyclic C_2H_6 adsorption performance, the sample was re-activated on the ASAP 2020 analyzer at 423 K for 6 h before subsequent adsorption analysis. Gas adsorption measurements adopted ultra-high purity grades N_2 (99.999%), C_2H_4

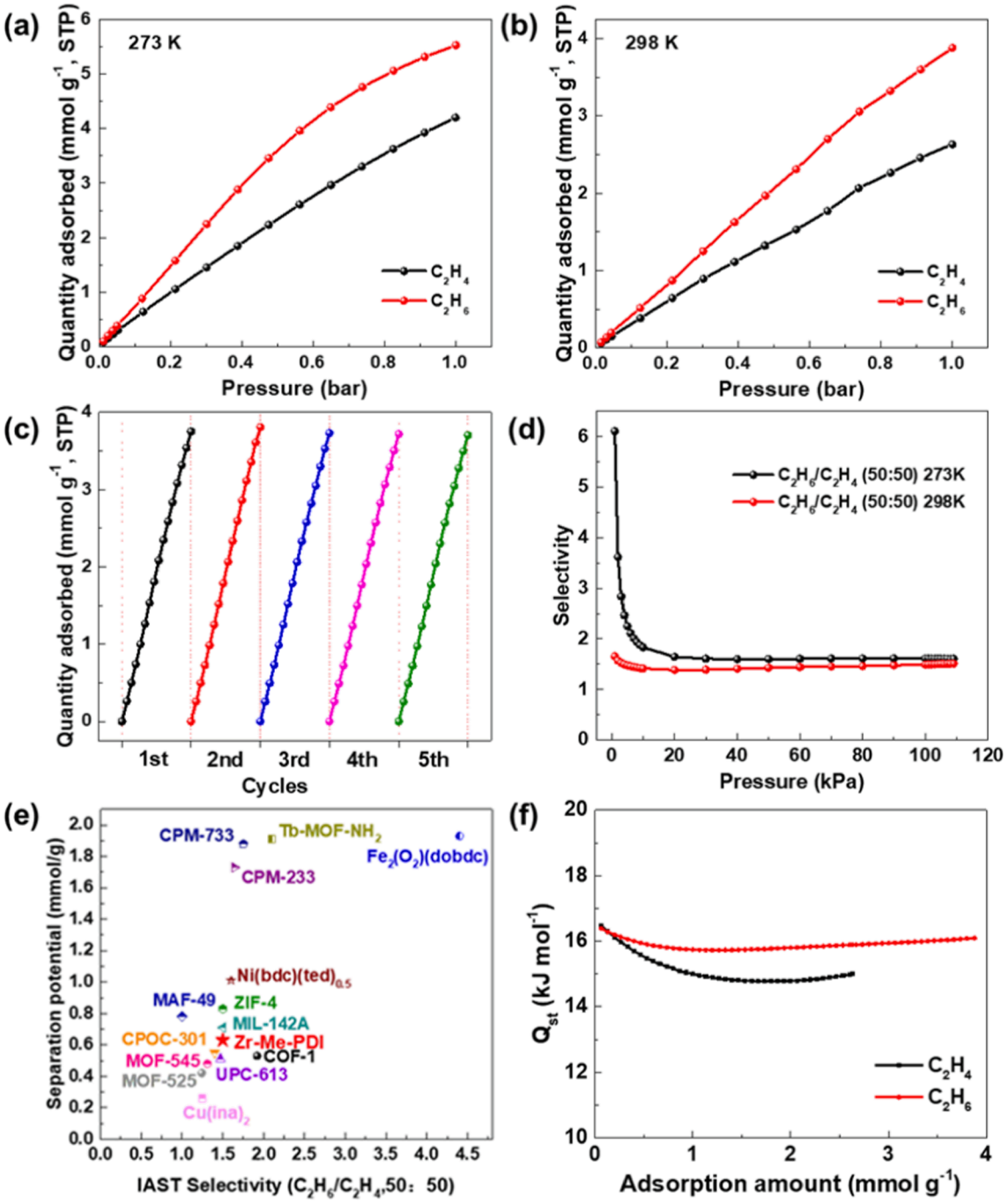

Fig. 3. (a-b) C_2H_6 and C_2H_4 adsorption isotherms for Zr-Me-PDI at 273 and 298 K. (c) Adsorption cycle of C_2H_6 by Zr-Me-PDI at 298 K. (d) The IAST selectivity of Zr-Me-PDI for C_2H_6 and C_2H_4 (50:50) mixtrues at 273 and 298 K. (e) IAST selectivity and Δq for the best C_2H_6-selective MOFs under ambient conditions. (f) The experimental Q_{st} for C_2H_6 and C_2H_4 on Zr-Me-PDI.

(99.99%) and C_2H_6 (99.99%).

2.3. Separation potential calculation

Separation potential (Δq) is a comprehensive index proposed by Krishna that combines adsorption capacity and selectivity to quantify mixture separations in fixed bed adsorbers [29,30]. The separation effect of different adsorbents can be evaluated by comparing the Δq directly.

For a C_2H_6/C_2H_4 mixture with a mole fraction of $y_{C_2H_6}$ and $y_{C_2H_4} = 1 - y_{C_2H_6}$, the weight Δq was calculated by ideal adsorbed solution theory (IAST) using the formula:

$$\Delta q = q_{C_2H_6}\frac{y_{C_2H_4}}{y_{C_2H_6}} - q_{C_2H_4}$$

where $q_{C_2H_6}$ and $q_{C_2H_4}$ are C_2H_6 and C_2H_4 absorption in the mixture, respectively, which are calculated based on IAST. For a 50/50 mixture, formula can be simplified as

$$\Delta q = q_{C_2H_6} - q_{C_2H_4}$$

The physical significance of Δq is that it represents the maximum amount of pure C_2H_4 that can be recovered during the adsorption phase of fixed-bed separation.

3. Results and discussion

3.1. Structural and surface properties of Zr-Me-PDI

Zr-Me-PDI was constructed by solvothermal reaction of $ZrCl_4$ and PDI-Me-COOH ligand in DMF and acetic acid (Fig. 1). We firstly checked the as-synthesized sample with powder X-ray diffraction (PXRD) and it was observed that the diffraction patterns was consistent with the simulated PXRD pattern of reported Zr-PDI (Fig. 2a) [31,32]. Besides, the unit cell of Zr-Me-PDI is also similar to Zr-PDI (Table S1). These results indicated that Zr-Me-PDI isoreticular to Zr-PDI of high purity has been successfully synthesized. Similar to Zr-PDI, the structure of Zr-Me-PDI involves 12-connected *hexa*-nuclear zirconium cluster with a chemical formula of $Zr_6(\mu_3\text{-}O)_4(\mu_3\text{-}OH)_4(COO)_{12}$ as secondary building units (SBUs), which are connected through PDI-Me-COOH ligand to form a 3D framework (Fig. 1c). The SBU is composed of six zirconium atoms assembled into an $Zr_6(\mu_3\text{-}O)_4(\mu_3\text{-}OH)_4$ core which are completely coordinated by eight carboxylate units from PDI-Me-COOH and 4 carboxylate units from acetic acids. From the topological perspective, the *hexa*-nuclear zirconium clusters can be regarded as 4-connecting nodes as the zirconium clusters are connected with adjacent ones with two PDI-Me-COOH ligands. Thus, the framework of Zr-Me-PDI can be simplified into a 4 connected uninodal net with a point symbol of which corresponds to a five-fold interpenetrated diamond (dia) topology according to ToposPro program. Special sites that decorated with O and Cl atoms from adjacent organic ligands are created imparted by the interpenetrated frameworks and these sites may facilitate the gas separation [33]. Zr-Me-PDI is a highly porous framework with solvent-accessible volumes of about 51.5 %, as estimated by Zeo++ software from the simulated crystal structure data. Zr-Me-PDI was further analyzed by Fourier transform infrared spectroscopy (FT-IR). The peak at 3060 cm^{-1} could be assigned to aromatic C–H stretching vibration. Peaks near 1600 and 1450 cm^{-1} could be ascribed to aromatic ring skeleton vibrations with the peaks at 2960 and 2910 cm^{-1} corresponding to the stretching vibration of C–H of methyl group of PDI-Me-COOH ligand. Besides, the in-plain bending vibration for C–H of methyl group appears at 1382 cm^{-1} (Figure S3). In ultraviolet–visible-near-infrared (UV–Vis-NIR) absorption spectrum, three characteristic peaks corresponding to PDI-Me-COOH ligand were observed for Zr-Me-PDI (Fig. 2b). The morphology of Zr-Me-PDI was verified by optical microscope (OM) and scanning electron microscopy (SEM) (Figures S4 and S5). OM and SEM images indicated the prepared Zr-Me-PDI was mostly spherical with a size of 15 μm. EDX spectroscopy and mapping were performed, with results displaying that O, Cl, Zr, N, C evenly distributed in Zr-Me-PDI (Figure S6).

N_2 adsorption analysis was used to analyze the permanent porosity of Zr-Me-PDI at 77 K (Fig. 2c). Zr-Me-PDI showed type I isotherm with steep nitrogen gas uptake under relative low pressure ($p/p_0 < 0.1$), indicating its permanent microporous structure (Fig. 2c). The saturated N_2 uptake of Zr-Me-PDI reached 178 $cm^3 \cdot g^{-1}$. Brunauer-Emmett-Teller (BET) surface area and pore volume were calculated to be 634 $m^2 \cdot g^{-1}$ and 0.25 $cm^3 \cdot g^{-1}$, respectively. Furthermore, the pore size distribution of Zr-Me-PDI was calculated by nonlocal density functional theory (NLDFT), and the result revealed one pore with size near 1.56 nm. Thermogravimetric analysis (TGA) were conducted to explore the thermostability of Zr-Me-PDI. Two obvious mass loss and two main differential thermogravimetric (DTG) peaks were obviously observed (Fig. 2d). Weight loss of Zr-Me-PDI before 200 °C was due to the presence of adsorbed water and some organic solvent molecules in the sample, while the weight loss between 400 and 600 °C was due to the skeleton collapse, and final weight loss of the sample reached equilibrium. The TGA and DTG results indicated Zr-Me-PDI could be stable up to 400 °C.

The water stability of Zr-Me-PDI is a key factor determining its recycling performance as there is inevitably some water vapor in the feedstock gases during the industrial C_2H_6/C_2H_4 separation process. We performed water stability tests by immersing Zr-Me-PDI into aqueous solutions of varied pH values (1.0 ~ 10.0) at room temperature for 24 h. By comparing PXRD patterns, it was observed that the diffraction peaks of the treated Zr-Me-PDI were well-matched with the as-synthesized one (Fig. 2a). This result indicates that the framework of Zr-Me-PDI is intact and maintains good crystallinity with no phase transformation observed. The superior stability could be ascribed to the multiple strong Zr-O interactions with the Zr-O bond energy is 776 kJ mol^{-1} [34,35]. Besides, the five-fold interpenetrated structure may also play an important role in maintaining its stability [36,37].

3.2. Adsorption performance of Zr-Me-PDI

The C_2H_6 and C_2H_4 pure-component adsorption isotherms for Zr-Me-PDI were recorded at 273 and 298 K. The uptake capacities of both C_2H_6 and C_2H_4 were observed to decrease with increasing temperature, which reflected the thermodynamic control of physical adsorption (Fig. 3a, 3b). Obviously, Zr-Me-PDI exhibited obvious C_2H_6-selective adsorption behaviour at both test temperatures. The adsorption capacity of Zr-Me-PDI for C_2H_6 was 3.9 $mmol \cdot g^{-1}$, 1.3 $mmol \cdot g^{-1}$ higher than the adsoprtion capacity for C_2H_4 at 1 bar and 298 K. The adsorption difference between C_2H_6 and C_2H_4 indicated that C_2H_6 instead of C_2H_4 is more preferentially adsorbed into the skeleton. The adsorption capacity of Zr-Me-PDI for C_2H_6 outperforms most reported C_2H_6-selective MOFs (Table S2), like CPOC-301 (3.8 $mmol \cdot g^{-1}$),[38] MIL-142A (3.8 $mmol \cdot g^{-1}$),[39] $Fe_2(O_2)$(dobdc) (3.4 $mmol \cdot g^{-1}$),[40] COF-1 (2.5 $mmol \cdot g^{-1}$),[41] EDLM (3.1 $mmol \cdot g^{-1}$)[28] and MAF-49 (1.7 $mmol \cdot g^{-1}$) [42] but inferior to several MOF materials, like SNNU-40 (4.9 $mmol \cdot g^{-1}$)[27] and Ni(bdc)(ted)$_{0.5}$ (5.0 $mmol \cdot g^{-1}$) [43]. It is worth to mention that no detectable loss is observed in C_2H_6 adsorption capacity at both 273 (Figure S7) and 298 K (Fig. 3c) even after performing five cycles of adsorption and desorption experiments.

According to the test results of pure-component gas adsorption performance, adsorptive selectivity for Zr-Me-PDI was calculated according to IAST (Figures S8-S11). The C_2H_6/C_2H_4 selectivity was computed to be 1.6 for 50/50 mixture at 1 bar and 273 K. The selectivity was slightly droped to 1.5 when increased the temperture to 298 K (Fig. 3d). By comparison, it can be found that the selectivity of Zr-Me-PDI at 1 bar and 298 K is superior to most reported MOFs (Table S2), like UPC-613 (1.47),[18] CPOC-301 (1.4),[38] MOF-545 (1.37),[44] MOF-525 (1.24),[18] Cu(ina)$_2$ (1.25),[45] lower than IRMOF-8 (1.8),[46] but

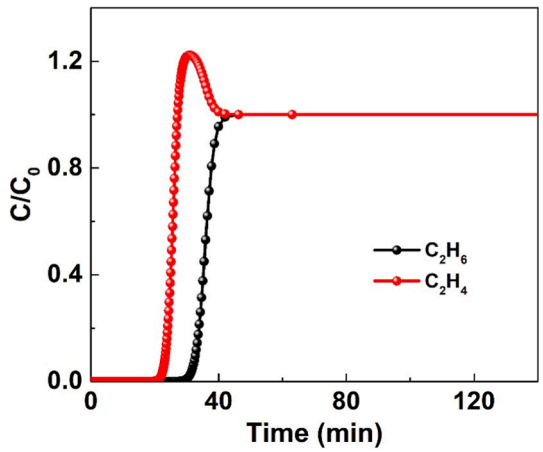

Fig. 4. Simulated column breakthrough curves of Zr-Me-PDI for the equimolar mixture of C_2H_6/C_2H_4 separation.

similar to ZIF-4 (1.5),[47] and MIL-142A (1.5) [39]. Typical reported C_2H_6-selective porous adsorbents are summarized (Figure S12 and Table S2). After comparing the C_2H_6 adsorption capacity and selectivity, it can be seen that Zr-Me-PDI can take into account better C_2H_6 adsorption capacity and excellent selectivity, which is superior to most of C_2H_6-selective porous adsorbents.

The Δq that combining the adsorption capacity and selectivity has been used to comprehensively evaluate the separation ability of adsorbents [48,49]. The Δq value for Zr-Me-PDI at 273 K was calculated to be 1.18 mmol·g^{-1}. The value was declined to 0.63 mmol·g^{-1} when the pure components adsorption isotherms that performed at 298 K was used for fitting. As displayed in Fig. 3e, the Δq for Zr-Me-PDI is superior to UPC-613 (0.51 mmol·g^{-1}),[18] and CPOC-301 (0.55 mmol·g^{-1}),[38] but lower than benchmark CMP-233 (1.73 mmol·g^{-1}),[21] CMP-733 (1.88 mmol·g^{-1}),[21] Tb-MOF-NH_2 (1.91 mmol·g^{-1}),[17] and $Fe_2(O_2)$(dobdc) (1.93 mmol·g^{-1}) [40]. However, the separation ability of Zr-Me-PDI may be compensated by its excellent stability under aqueous solution of different pH values.

Transient breakthrough simulation was carried out to validate the feasibility of using Zr-Me-PDI in a fixed bed for separation of C_2H_6/C_2H_4 (50/50, v/v) mixture. The methodology used in the breakthrough simulations is described in earlier works of Krishna [29,30]. In the breakthrough simulations, intra-crystalline diffusional influences are considered to be of negligible importance. As shown in Fig. 4., C_2H_4 is the first component to break through the fix bed adsorption column because of its weak affinity toward Zr-Me-PDI. The breakthrough time for C_2H_6 is longer than that of C_2H_4 and this result indicates the efficient separation of C_2H_6/C_2H_4 can be accomplished by Zr-Me-PDI. Next, the experimental transient breakthrough experiment was performed in a fixed bed to assess the separation performance of Zr-Me-PDI (Figure S13). There is a difference between the experimental breakthrough and the simulation one, which can be attributed to the existence of the kinetic effect or the difference in particle size, uniformity, and packing density [49,50].

The coverage dependent adsorption heat (Q_{st}) was also calculated to evaluate the binding affinity of Zr-Me-PDI towards C_2H_6 and C_2H_4. The Virial model was first adopted to fit the C_2H_6 and C_2H_4 adsorption isotherms at 273 and 298 K on Zr-Me-PDI with correlation coefficient values being 0.999 (Figures S14 and S15). Overall, the Q_{st} for C_2H_6 is higher than that of C_2H_4 (Fig. 3f). This also indicates that the material preferentially interacts with C_2H_6 molecules over C_2H_4, which is consistent with experimental test results. Besides, the Q_{st} value is far below the Q_{st} of the chemical adsorption, demonstrating that Zr-Me-PDI interacts moderately with C_2H_6 and C_2H_4 molecules, which is vitally important for adsorbents regeneration.

3.3. Proposed adsorption mechanism

In theory, determining gas adsorption sites in MOF framework is critical to guide the synthesis to high-performance MOF-based gas storage and separation materials. To elaborate the simultaneously high C_2H_6 adsorption capacity and gas pair C_2H_6/C_2H_4 selectivity in Zr-Me-PDI, GCMC simulations were conducted on Zr-Me-PDI to investigate the interaction discrepancies between these gas molecules and the framework at molecular level (Fig. 5). The emulation results indicate that the primary binding sites of molecules C_2H_6 and C_2H_4 are at polar pocket packed from three PDI-Me-COOH ligand. Only a single C_2H_6 or C_2H_4 molecule was exhibited at the adsorption site for clarity. The molecule C_2H_6 is bound to the Cl and O atoms from three neighboring PDI provided by interpenetrated frameworks, through three C-H···Cl hydrogen-bonding interactions with the H···Cl binding distances of 2.8467–3.1469 Å, and three C-H···O hydrogen-bonding interactions with the H···O binding distances of 2.6170–3.7766 Å. By contrast, molecule C_2H_4 is only show two C-H···Cl hydrogen-bonding interactions with the H···Cl binding distances of 3.1320–3.5532 Å, and two C-H···O hydrogen-bonding interactions with the H···O binding distances of 2.9756–3.7236 Å. Overall, the calculation result based on the number and distance of hydrogen bonds revealed that the formation of more multiple C-H···Cl and C-H···O hydrogen interactions between C_2H_6 and the interpenetrated framework of Zr-Me-PDI result in a stronger affinity towards C_2H_6 instead of C_2H_4. Such simulation results were fully consistent with the above-mentioned laboratorial observations, which can illustrate the preferential adsorption of C_2H_6 by Zr-Me-PDI.

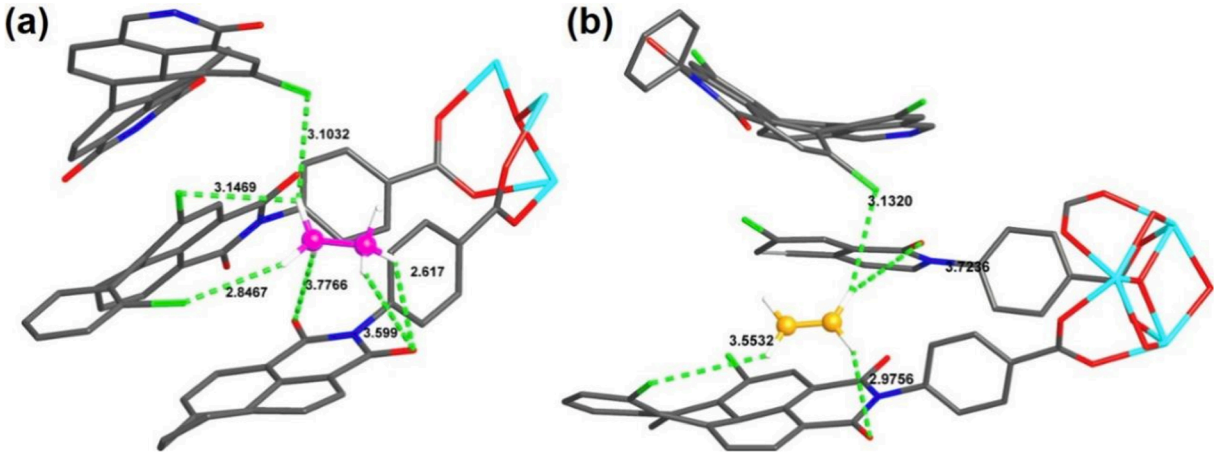

Fig. 5. Adsorption sites of (a) C_2H_6 and (b) C_2H_4 in Zr-Me-PDI identified using GCMC simulations.

4. Conclusions

In conclusion, robust Zr-Me-PDI was successfully prepared for C_2H_6 and C_2H_4 selective separation. Experimental results indicate Zr-Me-PDI possesses good stability under aqueous solution of different pH values. The pure-component gas isotherms experiments can confirm its preferential adsorption of C_2H_6 over C_2H_4 in Zr-Me-PDI. Specifically, the adsorption capacity of Zr-Me-PDI for C_2H_6 reached 3.9 mmol·g^{-1}, and the selectivity reached 1.5 at 1 bar and 298 K. Additionally, GCMC simulation indicated that interpenetrated structure of Zr-Me-PDI imparted more interaction affinity for C_2H_6 compared with C_2H_4 via crossing organic linker. Our work sheds light on design of stable PDI-based MOFs materials toward C_2H_4 purification.

CRediT authorship contribution statement

Jing-Jing Li: Investigation, Data curation, Visualization, Validation, Writing – original draft, Writing – review & editing. **Si-Yi Liu:** Investigation, Formal analysis. **Guoliang Liu:** Investigation, Methodology, Data curation, Writing – original draft, Writing – review & editing, Funding acquisition. **Yu-Guo Liu:** Investigation, Formal analysis, Data curation, Validation. **Guan-Zhou Wu:** Investigation, Formal analysis, Data curation. **Hua-Dong Li:** Investigation, Formal analysis, Data curation. **Rajamani Krishna:** . **Xiao-Qin Liu:** Validation. **Lin-Bing Sun:** Conceptualization, Methodology, Writing – review & editing, Funding acquisition, Supervision.

Declaration of Competing Interest

The authors declare that they have no known competing financial interests or personal relationships that could have appeared to influence the work reported in this paper.

Data availability

Data will be made available on request.

Acknowledgment

We acknowledge the financial support of this work by the National Key R&D Program of China (2022YFB3806800), the National Science Fund for Distinguished Young Scholars (22125804) and the National Natural Science Foundation of China (22001122 and 22078155).

Appendix A. Supplementary data

Supplementary data to this article can be found online at https://doi.org/10.1016/j.seppur.2023.124109.

References

[1] X. Pan, F. Jiao, D. Miao, X. Bao, Oxide-zeolite-based composite catalyst concept that enables syngas chemistry beyond fischer-tropsch synthesis, Chem. Rev. 121 (2021) 6588–6609.
[2] G. Luongo, F. Donat, A.H. Bork, E. Willinger, A. Landuyt, C.R. Muller, Highly selective oxidative dehydrogenation of ethane to ethylene via chemical looping with oxygen uncoupling through structural engineering of the oxygen carrier, Adv. Energy Mater. 12 (2022) 2200405.
[3] Q. Ding, Z. Zhang, Y. Liu, K. Chai, R. Krishna, S. Zhang, One-step ethylene purification from ternary mixtures in a metal-organic framework with customized pore chemistry and shape, Angew. Chem. Int. Ed. 61 (2022) e202208134.
[4] Z. Di, C. Liu, J. Pang, S. Zou, Z. Ji, F. Hu, C. Chen, D. Yuan, M. Hong, M. Wu, A metal-organic framework with nonpolar pore surfaces for the one-step acquisition of C_2H_4 from a C_2H_4 and C_2H_6 mixture, Angew. Chem. Int. Ed. 61 (2022) e202210343.
[5] Q. Hong, W. Wang, S. Chen, K. Chen, M. Liu, H.-X. Zhang, J. Zhang, Host-guest pore space partition in a boron imidazolate framework for ethylene separation, Chem. Mater. 34 (2021) 307–313.
[6] J. Pei, J.-X. Wang, K. Shao, Y. Yang, Y. Cui, H. Wu, W. Zhou, B. Li, G. Qian, Engineering microporous ethane-trapping metal-organic frameworks for boosting ethane/ethylene separation, J. Mater. Chem. A 8 (2020) 3613–3620.
[7] Z. Bao, G. Chang, H. Xing, R. Krishna, Q. Ren, B. Chen, Potential of microporous metal-organic frameworks for separation of hydrocarbon mixtures, Energy Environ. Sci. 9 (2016) 3612–3641.
[8] Y. Chen, Z. Qiao, H. Wu, D. Lv, R. Shi, Q. Xia, J. Zhou, Z. Li, An ethane-trapping MOF PCN-250 for highly selective adsorption of ethane over ethylene, Chem. Eng. Sci. 175 (2018) 110–117.
[9] M. Oschatz, M. Antonietti, A search for selectivity to enable CO_2 capture with porous adsorbents, Energy Environ. Sci. 11 (2018) 57–70.
[10] Y. Wang, S.B. Peh, D. Zhao, Alternatives to cryogenic distillation: Advanced porous materials in adsorptive light olefin/paraffin separations, Small 15 (2019) e1900058.
[11] W.G. Cui, T.L. Hu, X.H. Bu, Metal-organic framework materials for the separation and purification of light hydrocarbons, Adv. Mater. 32 (2020) e1806445.
[12] G. Liu, M. Zhou, K. Su, R. Babarao, D. Yuan, M. Hong, Stabilizing the extrinsic porosity in metal-organic cages-based supramolecular framework by in situ catalytic polymerization, CCS Chem. 3 (2021) 1382–1390.
[13] D. Wu, P.-F. Zhang, G.-P. Yang, L. Hou, W.-Y. Zhang, Y.-F. Han, P. Liu, Y.-Y. Wang, Supramolecular control of MOF pore properties for the tailored guest adsorption/separation applications, Coord. Chem. Rev. 434 (2021) 213709.
[14] J. Liu, J. Miao, S. Ullah, K. Zhou, L. Yu, H. Wang, Y. Wang, T. Thonhauser, J. Li, A water-resistant hydrogen-bonded organic framework for ethane/ethylene separation in humid environments, ACS Mater. Lett. 4 (2022) 1227–1232.
[15] X.W. Gu, J. Pei, K. Shao, H.M. Wen, B. Li, G. Qian, Chemically stable hafnium-based metal-organic framework for highly efficient C_2H_6/C_2H_4 separation under humid conditions, ACS Appl. Mater. Interfaces 13 (2021) 18792–18799.
[16] J.-X. Wang, X.-W. Gu, Y.-X. Lin, B. Li, G. Qian, A novel hydrogen-bonded organic framework with highly permanent porosity for boosting ethane/ethylene separation, ACS Mater. Lett. 3 (2021) 497–503.
[17] G.D. Wang, R. Krishna, Y.Z. Li, W.J. Shi, L. Hou, Y.Y. Wang, Z. Zhu, Boosting ethane/ethylene separation by MOFs through the amino-functionalization of pores, Angew. Chem. Int. Ed. 61 (2022) e202213015.
[18] Y. Wang, C. Hao, W. Fan, M. Fu, X. Wang, Z. Wang, L. Zhu, Y. Li, X. Lu, F. Dai, Z. Kang, R. Wang, W. Guo, S. Hu, D. Sun, One-step ethylene purification from an acetylene/ethylene/ethane ternary mixture by cyclopentadiene cobalt-functionalized metal-organic frameworks, Angew. Chem. Int. Ed. 60 (2021) 11350–11358.
[19] H. Park, M. Kang, D.W. Kang, C.S. Hong, A robust ethane-selective hypercrosslinked porous organic adsorbent with high ethane capacity, J. Mater. Chem. A 10 (2022) 3579–3584.
[20] F. Jin, E. Lin, T. Wang, S. Geng, T. Wang, W. Liu, F. Xiong, Z. Wang, Y. Chen, P. Cheng, Z. Zhang, Bottom-up synthesis of 8-connected three-dimensional covalent organic frameworks for highly efficient ethylene/ethane separation, J. Am. Chem. Soc. 144 (2022) 5643–5652.
[21] H. Yang, Y. Wang, R. Krishna, X. Jia, Y. Wang, A.N. Hong, C. Dang, H.E. Castillo, X. Bu, P. Feng, Pore-space-partition-enabled exceptional ethane uptake and ethane-selective ethane-ethylene separation, J. Am. Chem. Soc. 142 (2020) 2222–2227.
[22] Y. Yang, L. Li, R.B. Lin, Y. Ye, Z. Yao, L. Yang, F. Xiang, S. Chen, Z. Zhang, S. Xiang, B. Chen, Ethylene/ethane separation in a stable hydrogen-bonded organic framework through a gating mechanism, Nat. Chem. 13 (2021) 933–939.
[23] D. Lv, P. Zhou, J. Xu, S. Tu, F. Xu, J. Yan, H. Xi, W. Yuan, Q. Fu, X. Chen, Q. Xia, Recent advances in adsorptive separation of ethane and ethylene by C_2H_6-selective MOFs and other adsorbents, Chem. Eng. J. 431 (2022) 133208.
[24] L. Zhang, L. Li, E. Hu, L. Yang, K. Shao, L. Yao, K. Jiang, Y. Cui, Y. Yang, B. Li, B. Chen, G. Qian, Boosting ethylene/ethane separation within Copper(I)-chelated metal-organic frameworks through tailor-made aperture and specific π-complexation, Adv. Sci. 7 (2020) 1901918.
[25] M.H. Mohamed, Y. Yang, L. Li, S. Zhang, J.P. Ruffley, A.G. Jarvi, S. Saxena, G. Veser, J.K. Johnson, N.L. Rosi, Designing open metal sites in metal-organic frameworks for paraffin/olefin separations, J. Am. Chem. Soc. 141 (2019) 13003–13007.
[26] J.E. Bachman, M.T. Kapelewski, D.A. Reed, M.I. Gonzalez, J.R. Long, M2(m-dobdc) (M = Mn, Fe Co, Ni) metal-organic frameworks as highly selective, high-capacity adsorbents for olefin/paraffin separations, J. Am. Chem. Soc. 139 (2017) 15363–15370.
[27] Y.P. Li, Y.N. Zhao, S.N. Li, D.Q. Yuan, Y.C. Jiang, X. Bu, M.C. Hu, Q.G. Zhai, Ultrahigh-uptake capacity-enabled gas separation and fruit preservation by a new single-walled nickel-organic framework, Adv. Sci. 8 (2021) 2003141.
[28] P. Hu, J. Hu, H. Wang, H. Liu, J. Zhou, Y. Liu, Y. Wang, H. Ji, One-step ethylene purification by an ethane-screening metal-organic framework, ACS Appl. Mater. Interfaces 14 (2022) 15195–15204.
[29] R. Krishna, Screening metal-organic frameworks for mixture separations in fixed-bed adsorbers using a combined selectivity/capacity metric, RSC Adv. 7 (2017) 35724–35737.
[30] R. Krishna, Metrics for evaluation and screening of metal-organic frameworks for applications in mixture separations, ACS Omega 5 (2020) 16987–17004.
[31] B. Lu, Y. Chen, P. Li, B. Wang, K. Mullen, M. Yin, Stable radical anions generated from a porous perylenediimide metal-organic framework for boosting near-infrared photothermal conversion, Nat. Commun. 10 (2019) 767.
[32] Y.-G. Gu, G. Liu, P. Tan, C. Gu, J.-J. Li, X.-Q. Liu, L.-B. Sun, Near-infrared light triggered release of ethane from a photothermal metal-organic framework, Chem. Eng. J. 420 (2021) 130490.

[33] D. Lv, R. Shi, Y. Chen, Y. Wu, H. Wu, H. Xi, Q. Xia, Z. Li, Selective adsorption of ethane over ethylene in PCN-245: Impacts of interpenetrated adsorbent, ACS Appl. Mater. Interfaces 10 (2018) 8366–8373.
[34] H. Yuan, G. Liu, Z. Qiao, N. Li, P.J.S. Buenconsejo, S. Xi, A. Karmakar, M. Li, H. Cai, S.J. Pennycook, D. Zhao, Solution-processable metal-organic framework nanosheets with variable functionalities, Adv. Mater. 33 (2021) e2101257.
[35] G. Liu, Y. Di Yuan, J. Wang, Y. Cheng, S.B. Peh, Y. Wang, Y. Qian, J. Dong, D. Yuan, D. Zhao, Process-tracing study on the postassembly modification of highly stable zirconium metal-organic cages, J. Am. Chem. Soc. 140 (2018) 6231–6234.
[36] L. Robison, X. Gong, A.M. Evans, F.A. Son, X. Wang, L.R. Redfern, M.C. Wasson, Z. H. Syed, Z. Chen, K.B. Idrees, T. Islamoglu, M. Delferro, W.R. Dichtel, F.-X. Coudert, N.C. Gianneschi, O.K. Farha, Transient catenation in a zirconium-based metal-organic framework and its effect on mechanical stability and sorption properties, J. Am. Chem. Soc. 143 (2021) 1503–1512.
[37] Y. Qiao, X. Chang, J.Y. Zheng, M. Yi, Z. Chang, M.H. Yu, X.H. Bu, Self-interpenetrated water-stable microporous metal-organic framework toward storage and purification of light hydrocarbons, Inorg. Chem. 60 (2021) 2749–2755.
[38] K. Su, W. Wang, S. Du, C. Ji, D. Yuan, Efficient ethylene purification by a robust ethane-trapping porous organic cage, Nat. Commun. 12 (2021) 3703.
[39] Y. Chen, H. Wu, D. Lv, R. Shi, Y. Chen, Q. Xia, Z. Li, Highly adsorptive separation of ethane/ethylene by an ethane-selective MOF MIL-142A, Ind. Eng. Chem. Res. 57 (2018) 4063–4069.
[40] L. Li, R.B. Lin, R. Krishna, H. Li, S. Xiang, H. Wu, J. Li, W. Zhou, B. Chen, Ethane/ethylene separation in a metal-organic framework with iron-peroxo sites, Science 362 (2018) 443–446.
[41] C. He, Y. Wang, Y. Chen, X. Wang, J. Yang, L. Li, J. Li, Microregulation of pore channels in covalent-organic frameworks used for the selective and efficient separation of ethane, ACS Appl. Mater. Interfaces 12 (2020) 52819–52825.
[42] P.Q. Liao, W.X. Zhang, J.P. Zhang, X.M. Chen, Efficient purification of ethene by an ethane-trapping metal-organic framework, Nat. Commun. 6 (2015) 8697.
[43] W. Liang, F. Xu, X. Zhou, J. Xiao, Q. Xia, Y. Li, Z. Li, Ethane selective adsorbent Ni(bdc)(ted)$_{0.5}$ with high uptake and its significance in adsorption separation of ethane and ethylene, Chem. Eng. Sci. 148 (2016) 275–281.
[44] Y. Zhang, D. Lv, J. Chen, Z. Liu, C. Duan, X. Chen, W. Yuan, H. Xi, Q. Xia, Preferential adsorption of ethane over ethylene on a Zr-based metal-organic framework: Impacts of C-H···N hydrogen bonding, New J. Chem. 45 (2021) 8045–8053.
[45] R.B. Lin, H. Wu, L. Li, X.L. Tang, Z. Li, J. Gao, H. Cui, W. Zhou, B. Chen, Boosting ethane/ethylene separation within isoreticular ultramicroporous metal-organic frameworks, J. Am. Chem. Soc. 140 (2018) 12940–12946.
[46] J. Pires, M.L. Pinto, V.K. Saini, Ethane selective IRMOF-8 and its significance in ethane-ethylene separation by adsorption, ACS Appl. Mater. Interfaces 6 (2014) 12093–12099.
[47] M. Hartmann, U. Bohme, M. Hovestadt, C. Paula, Adsorptive separation of olefin/paraffin mixtures with ZIF-4, Langmuir 31 (2015) 12382–12389.
[48] Y. Jiang, J. Hu, L. Wang, W. Sun, N. Xu, R. Krishna, S. Duttwyler, X. Cui, H. Xing, Y. Zhang, Comprehensive pore tuning in an ultrastable fluorinated anion cross-linked cage-like MOF for simultaneous benchmark propyne recovery and propylene purification, Angew. Chem. Int. Ed. 61 (2022) e202200947.
[49] Y. Jiang, L. Wang, T. Yan, J. Hu, W. Sun, R. Krishna, D. Wang, Z. Gu, D. Liu, X. Cui, H. Xing, Y. Zhang, Insights into the thermodynamic-kinetic synergistic separation of propyne/propylene in anion pillared cage MOFs with entropy-enthalpy balanced adsorption sites, Chem. Sci. 14 (2023) 298–309.
[50] J. Pei, K. Shao, J.X. Wang, H.M. Wen, Y. Yang, Y. Cui, R. Krishna, B. Li, G. Qian, A chemically stable hofmann-type metal-organic framework with sandwich-like binding sites for benchmark acetylene capture, Adv. Mater. 32 (2020), e1908275.

Supporting Information

A robust perylene diimide-based zirconium metal-organic framework for preferential adsorption of ethane over ethylene

Jing-Jing Li[a], Si-Yi Liu[a], Guoliang Liu[a,], Yu-Guo Liu[a], Guan-Zhou Wu[a], Hua-Dong Li[a], Rajamani Krishna[b], Xiao-Qin Liu[a], and Lin-Bing Sun[a,*]*

[a] State Key Laboratory of Materials-Oriented Chemical Engineering, Jiangsu National Synergetic Innovation Center for Advanced Material (SICAM), College of Chemical Engineering, Nanjing Tech University, Nanjing 211816, China

[b] Van't Hoff Institute for Molecular Sciences, University of Amsterdam, Science Park 904, 1098 XH Amsterdam, Netherlands

**Corresponding authors. E-mail: glliu@njtech.edu.cn; lbsun@njtech.edu.cn.*

Materials

Zirconium (IV) chloride ($ZrCl_4$), 2-methyl-4-aminobenzoic acid were obtained from Sigma-Aldrich. 1,6,7, 12-tetrachloro-3,4,9, 10-perylene tetracarboxylic anhydride was purchased from Aladdin. Propionic acid, glacial acetic acid, ethanol, N, N-dimethylformamide, methanol (MeOH), dichloromethane (DCM) and chloroform were obtained from Sinopharm Chemical Reagent Co. Ltd. All chemicals were commercially available and used directly without further purification. Deionized water was used for all the experiments.

Synthesis of N, N'-bis-(2-methyl-4-benzoic acid)-1, 2, 6, 7-tetrachloropylene-3, 4, 9, 10-tetracarboxylic acid diimide (PDI-Me-COOH)

1,6,7,12-tetrachloro-3,4,9,10-perylene tetracarboxylic acid dianhydride (1.00 g, 1.89 mmol), 2-methyl-4-aminobenzoic acid (2.86 g, 18.90 mmol) and propionic acid (25 mL) were mixed in a round-bottom flask and stirred under reflux at 160 ºC for 16 h. The mixture was cooled to room temperature and 30 mL of water was added. The mixture was then filtered. The resulting solid was washed several times with DCM and MeOH (V: V=1:1). The solvent was removed in a vacuum drying oven to obtain a red powder (1.22 g, 94.90 %). The synthetic route of PDI-Me-COOH can be viewed in Scheme S1. The purity of PDI-Me-COOH was detected by ^{1}H NMR, as shown in Figure S2. ^{1}H NMR (400 MHz, DMSO-d_6): δ 13.06 (s, 2H), 8.62 (s, 4H), 8.00 (d, 2H), 7.40 (s, 4H), 2.59 (s, 6H).

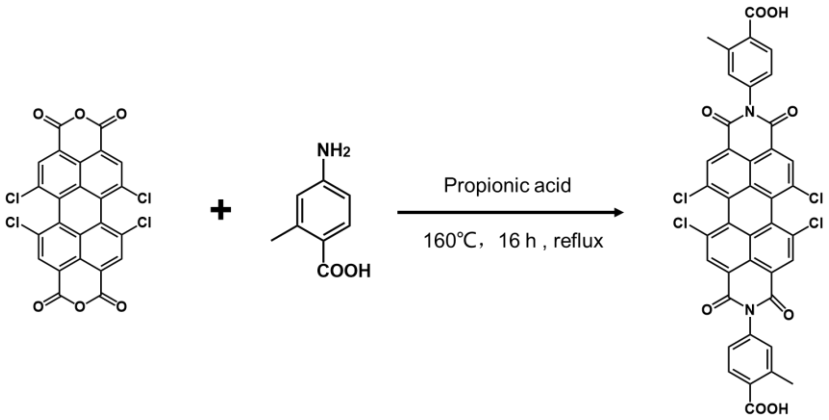

Scheme S1. The synthetic route of PDI-Me-COOH.

Structural Characterization

Powder X-ray diffraction (PXRD) patterns were recorded using an ARL EQUINOX 1000 diffractometer with monochromatic Cu Kα radiation in the 2θ range from 3° to 40°. SEM

images were performed on a Hitachi S4800 field emission scanning electron microscope. ^{1}H NMR spectrum of the samples was collected on a Bruker ACF-400 NMR Spectrometer. Fourier transform infrared spectroscopy (FT-IR) were carried out on a Nicolet Nexus 470 spectrometer. The ultraviolet-visible-near-infrared (UV-Vis-NIR) spectra were collected on the PerkinElmer Lambda 35 in the region of 300-1100 nm. The Brunauer-Emmett-Teller (BET) surface area was identified by the relative pressure ranging from 0.01 to 0.10. The total pore volume was analyzed by the uptake at a relative pressure of about 0.99. The pore size was calculated from the adsorption branch using a non-local density functional theory (NLDFT) method. Thermogravimetric analysis (TGA) was obtained on a STA-499 F3 synchronous thermal analyzer from Netzsch, Germany, at a heating rate of 20 °C/min under nitrogen atmosphere from room temperature to 900 °C. The derivatives (DTG) can be obtained by software analysis.

Selectivity Prediction for Binary Mixture Adsorption

The C_2H_6/C_2H_4 selectivity was calculated to evaluate the gas separation performance of Zr-Me-PDI. The dual-site Langmuir-Freundlich (DSLF) model and the theoretical adsorption solution theory (IAST) proposed by Myers et al.[1] were used to predict the selectivity of C_2H_6 and C_2H_4 mixtures on adsorbents at a certain mole fraction. The DSLF model for the site is:

$$y = A_1 \frac{b_1 x^{c_1}}{1 + b_1 x^{c_1}} + A_2 \frac{b_2 x^{c_2}}{1 + b_2 x^{c_2}}$$

Where y is the adsorption capacity (mmol/g); x is the pressure of the bulk gas in equilibrium with the adsorption phase (kPa), A_1 and A_2 are the saturated adsorption capacity of gas 1 at the two adsorption sites on the adsorbent (mmol/g), and b_1 and b_2 are the affinity constants of the two sites (kPa^{-1}). c_1 and c_2 are parameters that describe site heterogeneity. All fitted R coefficients were higher than 99.9%.

The fitted parameters were then applied to predict the adsorption selectivity of the IAST-based mixed C_2H_6/ C_2H_4. The adsorption selectivity is defined by the following equation:

$$S = \frac{x_i / x_j}{y_i / y_j}$$

where x_i and y_i represent the mole fraction of component i (i = 1, 2) in the adsorbed and bulk phases, respectively.

Isosteric Analysis of the Heat of Adsorption

In order to better understand the adsorption behavior of the adsorbent to the gas, we calculated the adsorption heat of the adsorbent. The adsorption heat analysis of the adsorbent to the gas is calculated according to the adsorption isotherm data of the gas at different temperatures, according to the virial equation:

$$\ln P = \ln N + \frac{1}{T}\sum_{i=0}^{m} a_i N^i + \sum_{i=0}^{n} b_i N^i$$

The expression for the heat of adsorption is:

$$Q_{st} = -R\sum_{i=0}^{m} a_i N^i$$

where P is the pressure (kPa), N is the adsorption amount ($mmol \cdot g^{-1}$), T is the adsorption temperature (K), R is the ideal gas constant (8.314 $J \cdot mol^{-1} \cdot K^{-1}$),m and n are the number of a and b parameters, respectively.

Transient breakthrough simulations

The performance of industrial fixed bed adsorbers is dictated by a combination of adsorption selectivity and uptake capacity. Transient breakthrough simulations were carried out for C_2H_6/C_2H_4 (v/v 50/50) mixtures operating at a total pressure of 100 kPa and 298 K, using the methodology described in earlier publications[2, 3]. For the breakthrough simulations, the same bed dimensions, flow rates, temperature and mass of adsorbent were used as in the experiments as described below. In the breakthrough simulations, intra-crystalline diffusion influences were considered to be of negligible importance.

Breakthrough experiment

In this project, the transient breakthrough experiments of Zr-Me-PDI was tested using a fixed bed. The breakthrough separation experiment was carried out at room temperature (298 K, 1 atm) by using C_2H_6/C_2H_4 (v/v=50/50) gas mixture in a quartz tube (6 mm inner diameter x 190 mm). The tube containing Zr-Me-PDI (800 mg) with a packed sample length of approximately 52 mm was pretreated with N_2 at 373 K for 120 min prior to the test. After the sample column is cooled to room temperature, the gas passing through the sample column is switched from N_2 to the mixture of C_2H_6/C_2H_4 (50:50) (2 mL/min). In the experiment, the gas

chromatography combined with thermal conductivity detector (TCD) and flame ionization detector (FID) was used to continuously monitor the gas at the exit of the adsorption column.

Grand Canonical Monte Carlo Calculations

The Grand Canonical Monte Carlo (GCMC) calculations,[4-6] performed by SORPTION code embedded in the Material Studio software, were carried out to study the C_2H_6/C_2H_4 adsorption capacity of Zr-Me-PDI at given 298 K and 1 atm pressure. The atomic locations were derived from the crystal data and calculated charges were applied. The C_2H_6 and C_2H_4 molecule was geometrically optimized by using the spin polarization density functional theory (DFT) on the basis of generalized gradient approximation (GGA) with the Perdew-Burke-Ernzerhof (PBE) function. The double numerical plus polarization (DNP) basis 3.5 and DFT Semi-Core Pseudopots treatment were adopted. In the simulations, we have modeled the framework and gas molecule as rigid and the universal force field (UFF) was applied. Cutoff distance was set to 18.5 Å for the Lennard-Jones (LJ) interactions. The van der Waals interactions and electrostatic interactions were dealt with the Atom based and Ewald summation method. The favorable adsorption sites were simulated by the Locate task. The loading steps, equilibration steps, and production steps were all set to 2×10^7. The snapshot for C_2H_6 and C_2H_4 adsorption at high loading under room temperature was calculated by the Fix pressure task in the sorption model.

Additional Figures

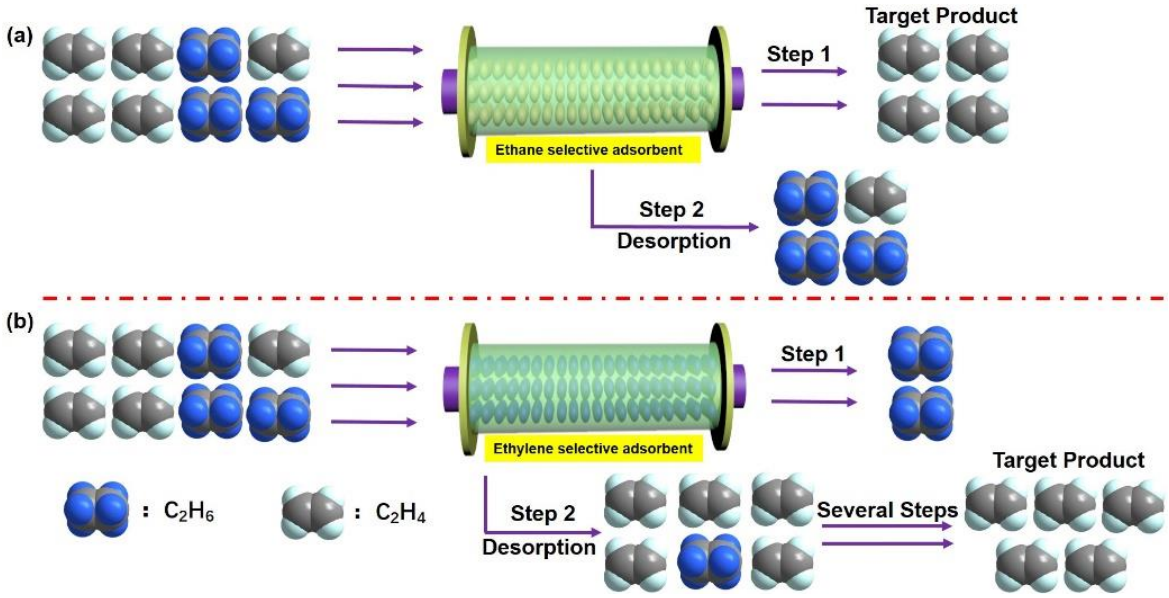

Figure S1. Schematic of the adsorptive separation process using ethane-selective MOFs adsorbent (a) and ethylene selective MOFs adsorbent (b).

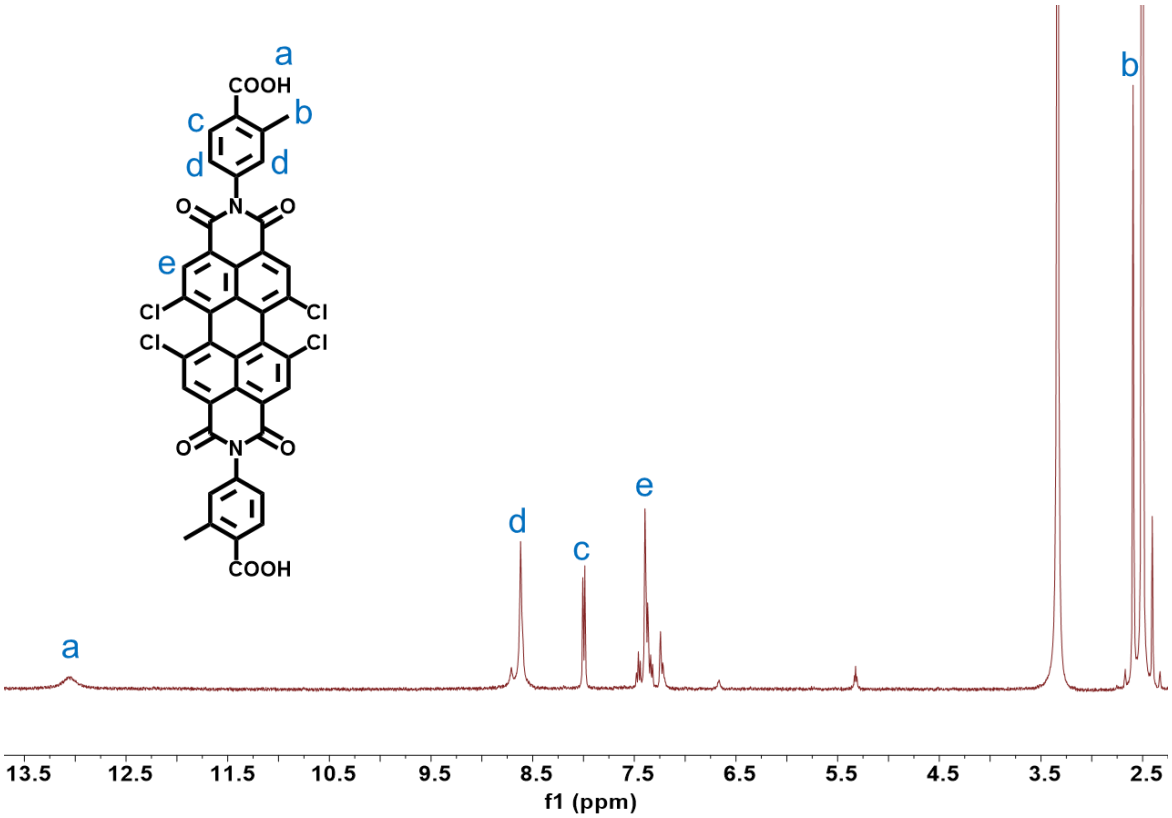

Figure S2. ^{1}H NMR spectrum of PDI-Me-COOH.

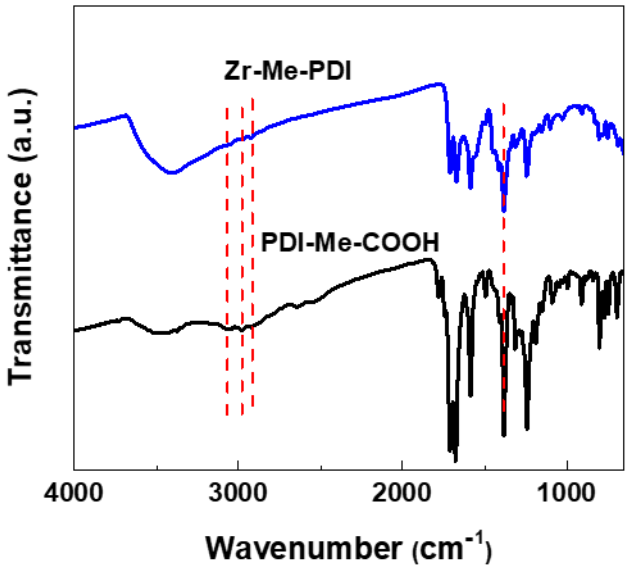

Figure S3. FT-IR spectra of PDI-Me-COOH and Zr-Me-PDI.

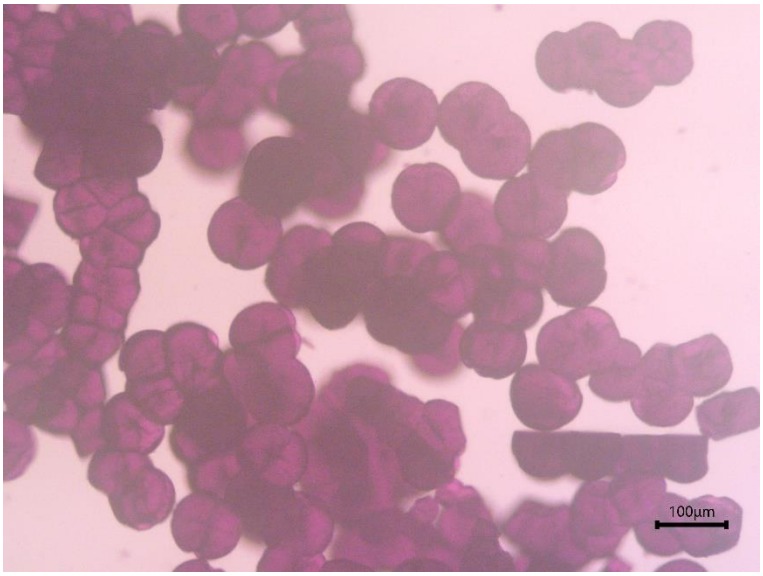

Figure S4. Optical micrograph image of Zr-Me-PDI.

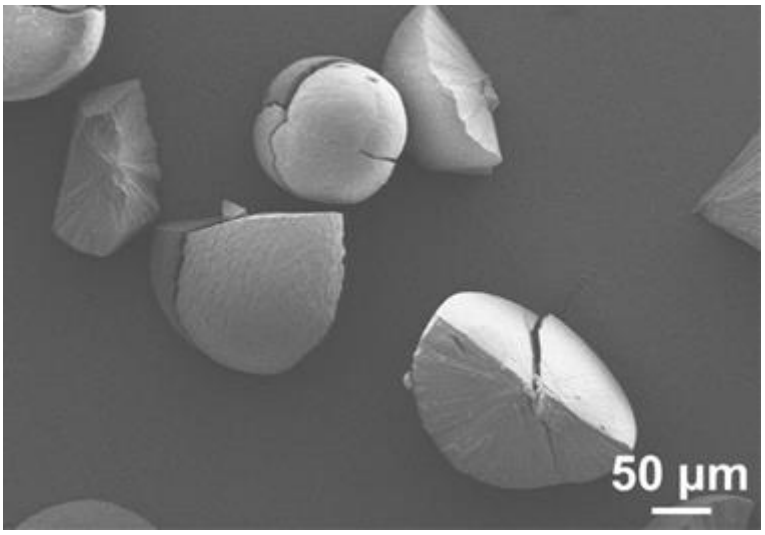

Figure S5. SEM image of Zr-Me-PDI.

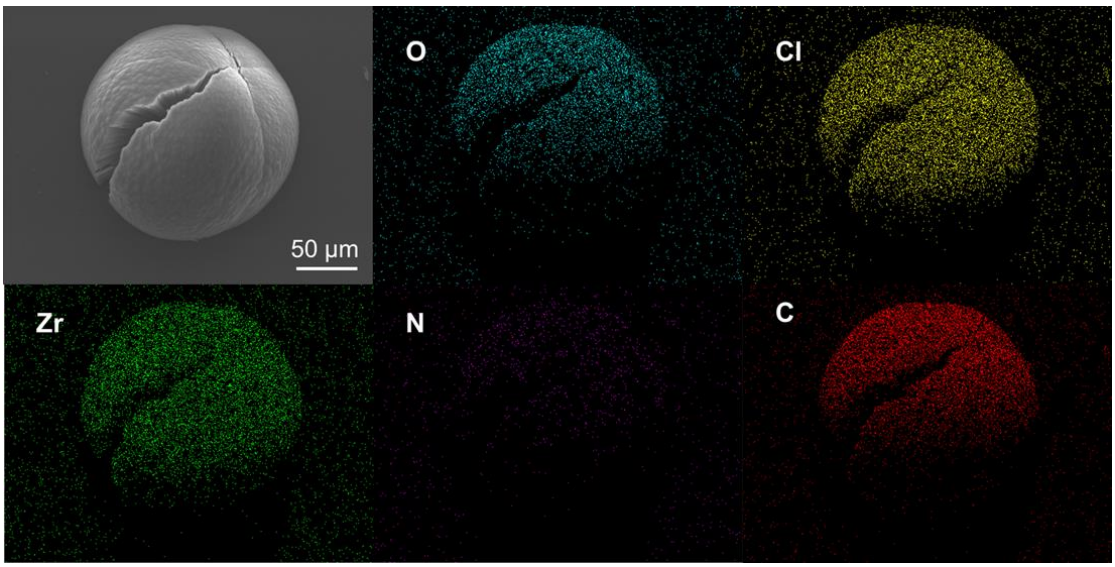

Figure S6. SEM images of Zr-Me-PDI as well as EDX-mapping images of C, N, O, Cl, and Zr elements.

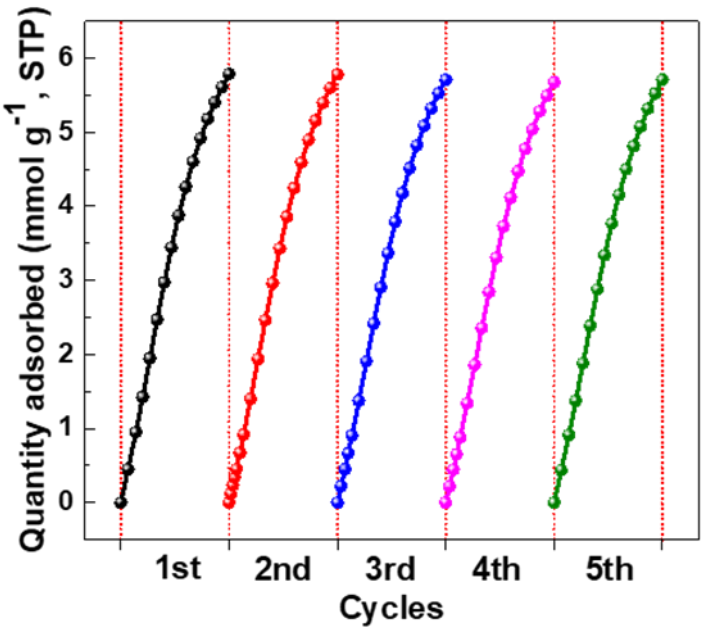

Figure S7. Adsorption cycles of C_2H_6 by Zr-Me-PDI at 273 K.

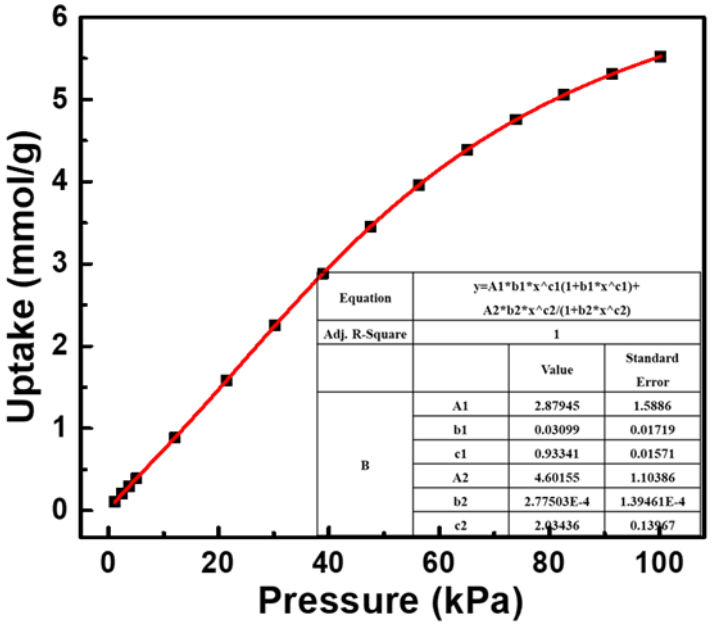

Figure S8. The parameters and optimized adsorption isotherm of C_2H_6 for calculated selectivity by using IAST at 273 K.

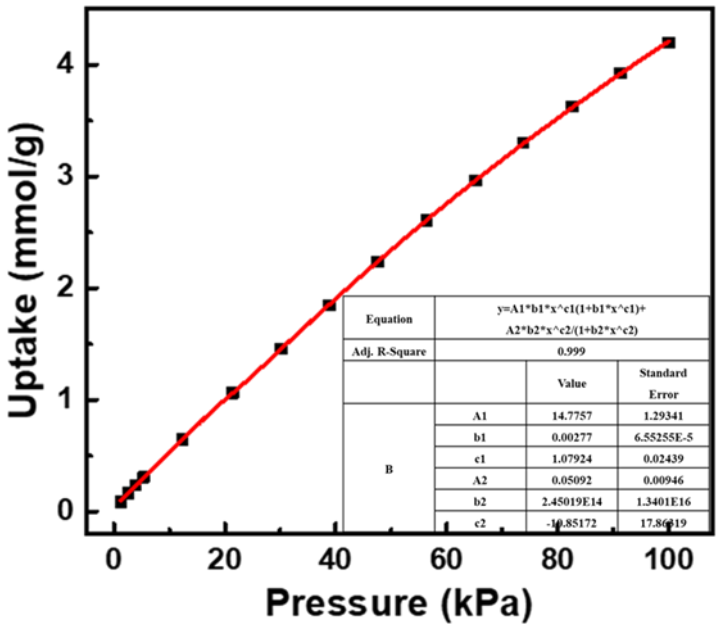

Figure S9. The parameters and optimized adsorption isotherm of C_2H_4 for calculated selectivity by using IAST at 273 K.

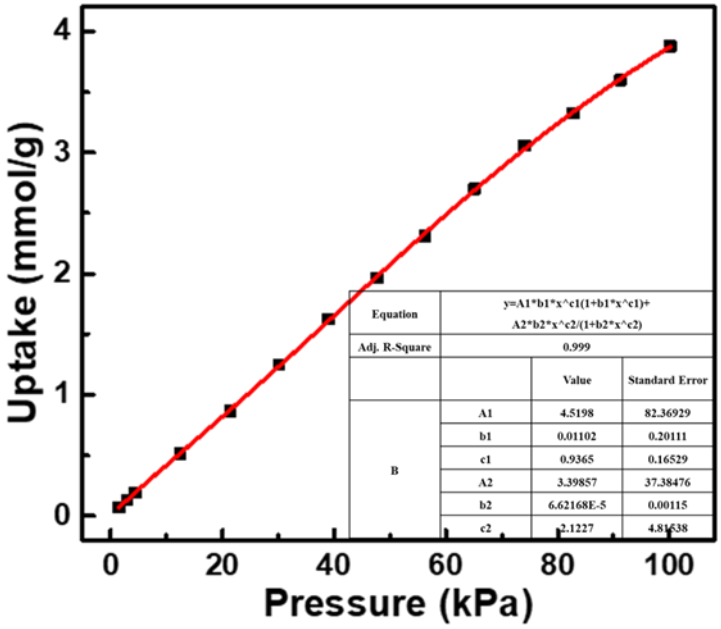

Figure S10. The parameters and optimized adsorption isotherm of C_2H_6 for calculated selectivity by using IAST at 298 K.

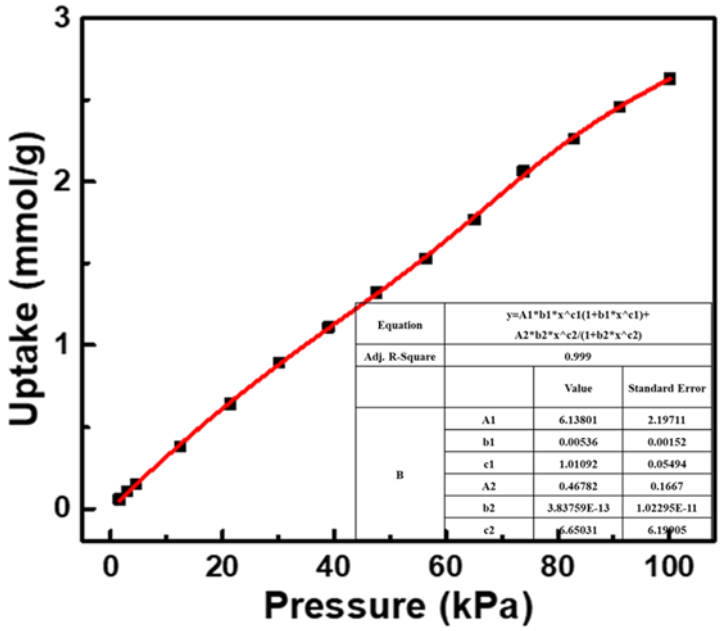

Figure S11. The parameters and optimized adsorption isotherm of C_2H_4 for calculated selectivity by using IAST at 298 K.

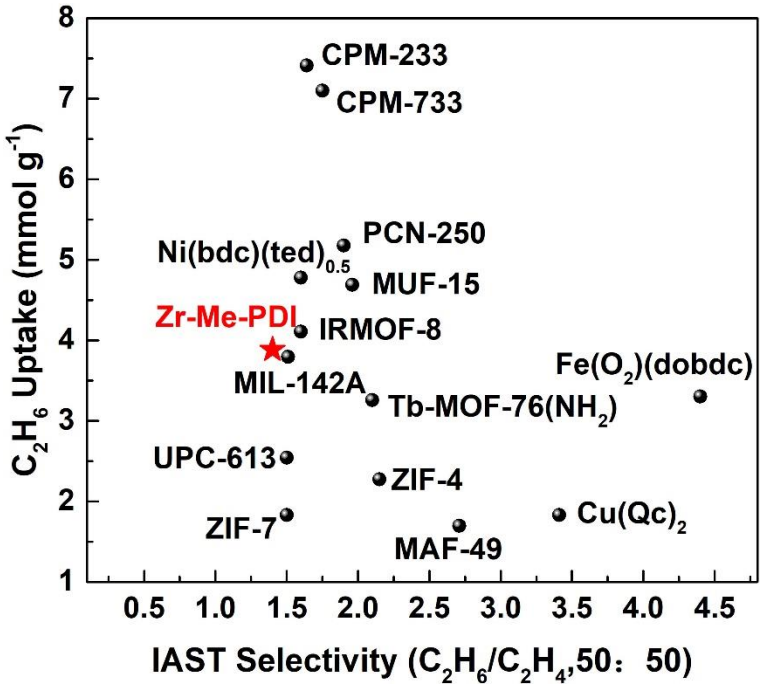

Figure S12. IAST selectivity and C_2H_6 adsorption capacity for the best C_2H_6-selective MOFs under ambient conditions.

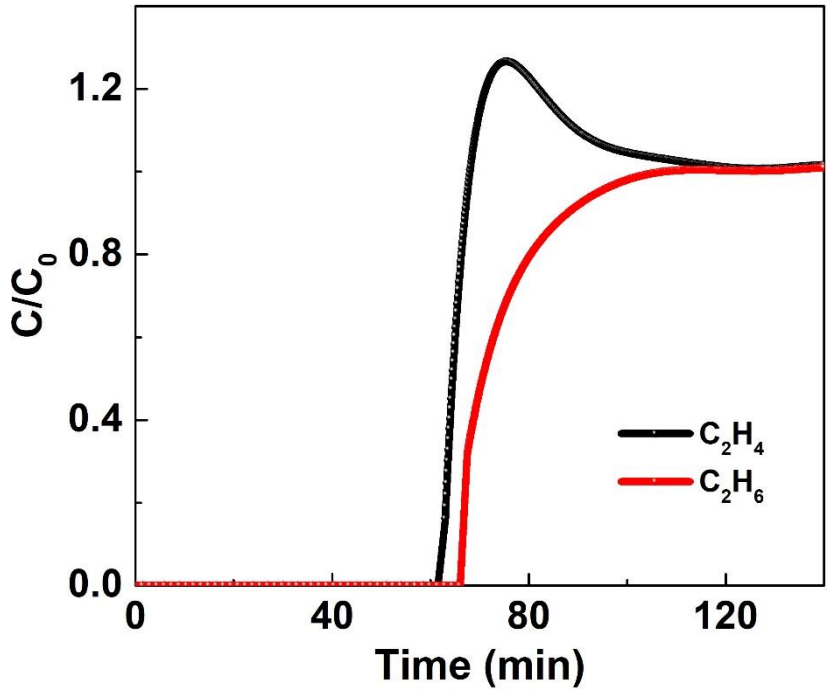

Figure S13. Experimental column breakthrough curves of Zr-Me-PDI for the equimolar mixture of C_2H_6/C_2H_4 separation.

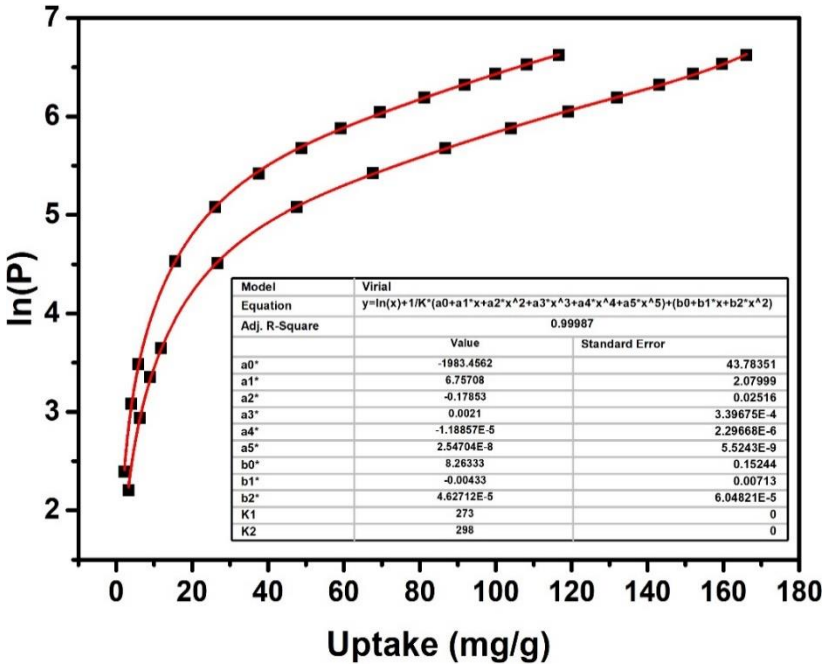

Model	Virial	
Equation	y=ln(x)+1/K*(a0+a1*x+a2*x^2+a3*x^3+a4*x^4+a5*x^5)+(b0+b1*x+b2*x^2)	
Adj. R-Square	0.99987	
	Value	Standard Error
a0*	-1983.4562	43.78351
a1*	6.75708	2.07999
a2*	-0.17853	0.02516
a3*	0.0021	3.39675E-4
a4*	-1.18857E-5	2.29668E-6
a5*	2.54704E-8	5.5243E-9
b0*	8.26333	0.15244
b1*	-0.00433	0.00713
b2*	4.62712E-5	6.04821E-5
K1	273	0
K2	298	0

Figure 14. Global Virial fitting curves of C_2H_6 on Zr-Me-PDI at different temperatures and the table list of corresponding fitting parameters.

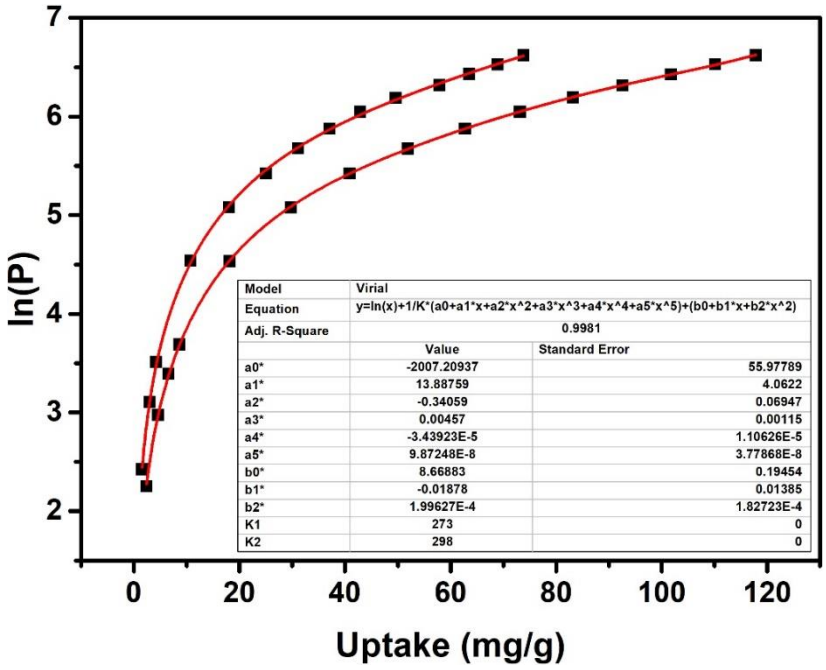

Model	Virial	
Equation	y=ln(x)+1/K*(a0+a1*x+a2*x^2+a3*x^3+a4*x^4+a5*x^5)+(b0+b1*x+b2*x^2)	
Adj. R-Square	0.9981	
	Value	Standard Error
a0*	-2007.20937	55.97789
a1*	13.88759	4.0622
a2*	-0.34059	0.06947
a3*	0.00457	0.00115
a4*	-3.43923E-5	1.10626E-5
a5*	9.87248E-8	3.77868E-8
b0*	8.66883	0.19454
b1*	-0.01878	0.01385
b2*	1.99627E-4	1.82723E-4
K1	273	0
K2	298	0

Figure 15. Global Virial fitting curves of C_2H_4 on Zr-Me-PDI at different temperatures and the table list of corresponding fitting parameters.

Table S1. Crystal structure for Zr-Me-PDI.

Identification code	Zr-Me-PDI
Temperature/K	298.15
Crystal system	tetragonal
Space group	$I4_1/a$
a/Å	18.080(4)
b/Å	18.110(5)
c/Å	86.530(2)
α/°	90
β/°	90
γ/°	90
Volume/Å^3	28333(13)
ρ_{calc}g/cm^3	0.983

Table S2. Comparison of C_2H_6 and C_2H_4 adsorption uptakes and selectivity of C_2H_6/C_2H_4 (50:50) in typical C_2H_6-selective adsorbents at 1 bar.

Adsorbents	Temperature (K)	C_2H_6 uptake (mmol/g)	C_2H_4 uptake (mmol/g)	Separation potential Δq (mmol/g)	C_2H_6/C_2H_4 selectivity	Reference
$Fe_2(O_2)(dobdc)$	298	3.32	2.63	1.93	4.4	[7]
$Ni(bdc)(ted)_{0.5}$	298	4.8	3.3	1.01	1.6	[8]
MAF-49	316	1.7	1.7	0.78	1.0	[9]
ZIF-4	293	2.2	2.0	0.83	1.5	[10]
CPOC-301	293	3.8	3.3	0.55(295K)	1.4	[11]
MOF-525	298	2.77	2.1	0.42(283K)	1.24	[12]
$Cu(ina)_2$	298	1.99	1.9	0.26	1.25	[13]
MIL-142A	298	3.8	2.9	0.71	1.5	[14]
UPC-613	298	2.56	2.25	0.51	1.47	[12]
Tb-MOF-NH_2	298	3.27	2.97	1.91	2.1	[15]
MOF-545	298	3.12	2.57	0.48	1.31	[16]
COF-1	298	2.46	1.92	0.53	1.92	[17]
CPM-233	298	7.45	6.52	1.73	1.64	[18]
CPM-733	298	7.13	6.37	1.88	1.75	[18]
Zr-Me-PDI	298	3.9	2.6	0.63	1.5	This work

References

[1] Walton, K. S., Sholl, D. S., Predicting Multicomponent Adsorption: 50 Years of the Ideal Adsorbed Solution Theory. *AIChE J.* **2015**, *61*, 2757-2762.

[2] Krishna, R., Screening Metal-Organic Frameworks for Mixture Separationsin Fixed-Bed Adsorbers Using a Combined Selectivity Capacity Metric. *RSC Adv.* **2017**, *7*, 35724-35737.

[3] Krishna, R., Metrics for Evaluation and Screening of Metal-Organic Frameworks for Applications in Mixture Separations. *ACS Omega.* **2020**, *5*, 16987-17004.

[4] Grosjean, B.; Pean, C.; Siria, A.; Bocquet, L.; Vuilleumier, R.; Bocquet, M., Chemisorption of Hydroxide on 2D Materials from DFT Calculations: Graphene Versus Hexagonal Boron Nitride. *J. Phys. Chem. Lett.* **2016**, *7*, 4695-4700.

[5] Fan, W.; Peh, S. B.; Zhang, Z.; Yuan, H.; Yang, Z.; Wang, Y.; Chai, K.; Sun, D.; Zhao, D., Tetrazole-Functionalized Zirconium Metal-Organic Cages for Efficient C_2H_2/C_2H_4 and C_2H_2/CO_2 Separations. *Angew. Chem. Int. Ed.* **2021**, *60*, 17338-17343.

[6] Wang, Y.; Hao, C.; Fan, W.; Fu, M.; Wang, X.; Wang, Z.; Zhu, L.; Li, Y.; Lu, X.; Dai, F.; Kang, Z.; Wang, R.; Guo, W.; Hu, S.; Sun, D., One-step Ethylene Purification from an Acetylene/Ethylene/Ethane Ternary Mixture by Cyclopentadiene Cobalt Functionalized Metal-Organic Frameworks. *Angew. Chem. Int. Ed.* **2021**, *60*, 11350-11358.

[7] Li, L.; Lin, R.-B.; Krishna, R.; Li, H.; Xiang, S.; Wu, H.; Li, J.; Zhou, W.; Chen, B., Ethane/Ethylene Separation in a Metal-Organic Framework with Iron-Peroxo Sites. *Science* **2018**, *362*, 443-446.

[8] Liang, W.; Xu, F.; Zhou, X.; Xiao, J.; Xia, Q.; Li, Y.; Li, Z., Ethane Selective Adsorbent $Ni(bdc)(ted)_{0.5}$ with High Uptake and its Significance in Adsorption Separation of Ethane and Ethylene. *Chem. Eng. Sci.* **2016**, *148*, 275-281.

[9] Liao, P. Q.; Zhang, W. X.; Zhang, J. P.; Chen, X. M., Efficient Purification of Ethene by an Ethane-Trapping Metal-Organic Framework. *Nat. Commun.* **2015**, *6*, 8697.

[10] Hartmann, M.; Bohme, U.; Hovestadt, M.; Paula, C., Adsorptive Separation of Olefin/Paraffin Mixtures with ZIF-4. *Langmuir* **2015**, *31*, 12382-12389.

[11] Su, K.; Wang, W.; Du, S.; Ji, C.; Yuan, D., Efficient Ethylene Purification by a Robust Ethane-Trapping Porous Organic Cage. *Nat. Commun.* **2021**, *12*, 3703.

[12] Wang, Y.; Hao, C.; Fan, W.; Fu, M.; Wang, X.; Wang, Z.; Zhu, L.; Li, Y.; Lu, X.; Dai, F.; Kang, Z.; Wang, R.; Guo, W.; Hu, S.; Sun, D., One-step Ethylene Purification from an Acetylene/Ethylene/Ethane Ternary Mixture by Cyclopentadiene Cobalt-Functionalized Metal-Organic Frameworks. *Angew. Chem. Int. Ed.* **2021**, *60*, 11350-11358.

[13] Lin, R. B.; Wu, H.; Li, L.; Tang, X. L.; Li, Z.; Gao, J.; Cui, H.; Zhou, W.; Chen, B., Boosting Ethane/Ethylene Separation within Isoreticular Ultramicroporous Metal-Organic Frameworks. *J. Am. Chem. Soc.* **2018**, *140*, 12940-12946.

[14] Chen, Y.; Wu, H.; Lv, D.; Shi, R.; Chen, Y.; Xia, Q.; Li, Z., Highly Adsorptive Separation of Ethane/Ethylene by An Ethane-Selective MOF MIL-142A. *Ind. Eng. Chem. Res.* **2018**, *57*, 4063-4069.

[15] Wang, G. D.; Krishna, R.; Li, Y. Z.; Shi, W. J.; Hou, L.; Wang, Y. Y.; Zhu, Z., Boosting Ethane/Ethylene Separation by MOFs through the Amino-Functionalization of Pores. *Angew. Chem. Int. Ed.* **2022**, *134*. e202213015.

[16] Zhang, Y.; Lv, D.; Chen, J.; Liu, Z.; Duan, C.; Chen, X.; Yuan, W.; Xi, H.; Xia, Q., Preferential Adsorption of Ethane over Ethylene on a Zr-Based Metal-Organic Framework:

Impacts of C-H···N Hydrogen Bonding. *New J. Chem.* **2021**, *45*, 8045-8053.

[17] Hu, P.; Hu, J.; Wang, H.; Liu, H.; Zhou, J.; Liu, Y.; Wang, Y.; Ji, H., One-Step Ethylene Purification by an Ethane-Screening Metal-Organic Framework. *ACS Appl. Mater. Interfaces* **2022**, *14*, 15195-15204.

[18] Yang, H.; Wang, Y.; Krishna, R.; Jia, X.; Wang, Y.; Hong, A. N.; Dang, C.; Castillo, H. E.; Bu, X.; Feng, P., Pore-Space-Partition-Enabled Exceptional Ethane Uptake and Ethane-Selective Ethane-Ethylene Separation. *J. Am. Chem. Soc.* **2020**, *142*, 2222-2227.